https://doi.org/10.5194/egusphere-2026-3404
Preprint. Discussion started: 10 July 2026

Design of a Cloud Chamber and Quantitative Seeding Experiments for Warm and Cold Clouds

Jiayi Luo[1], Haopeng Zhang[1], Yuan Jiang[2], Hao Wu[1]

[1]Key Laboratory of China Meteorological Administration Atmospheric Sounding, School of Electrical Engineering, Chengdu University of Information Technology, Chengdu 610225, China
[2]College of Resources and Environment, Chengdu University of Information Technology, Chengdu 610225, China

Correspondence to: Hao Wu (wuhao@cuit.edu.cn)

Abstract. Cloud chambers provide controlled thermodynamic environments for investigating cloud microphysical processes and their responses to aerosol perturbations. In this study, we developed a cloud chamber system for controlled observations of cloud microphysics and weather-modification processes. The system comprises two vessels with volumes of 2.7 and 9.0 m³. It provides adjustable temperature and pressure over approximate ranges of -40 to 40 °C and 30 to 1100 hPa, respectively, and is designed to regulate relative humidity across nearly the full 0 to 100 % range. The measurement system covers particles from submicron aerosols to cloud and precipitation particles, with approximate size ranges of 10-700 nm for submicron aerosols and 2-1550 μm for cloud droplets, larger hydrometeors, and ice particles. The chamber performance was evaluated using temperature-control, pressure-control, and humidity-control tests. Representative paired background–seeded experiments were then conducted in chamber B under warm-cloud and cold-cloud conditions. In the warm-cloud experiment, the introduction of 10 g of hygroscopic seeding powder increased the aerosol number concentration and was accompanied by a rapid increase in 3-10 μm droplets. Relative to the background case, the seeded case had a lower concentration of droplets ≥12 μm, with the mean concentration decreasing from 1357 to 478 cm^{-3}, and showed shorter cloud persistence. The relative-humidity decline rate was higher in the seeded case than in the background case, increasing from 0.47 to 0.75 % RH min^{-1}, consistent with enhanced water-vapour uptake after the introduction of hygroscopic particles. In the cold-cloud experiment, 0.5 g of AgI was ignited, and the resulting AgI-containing combustion aerosol increased the submicron particle concentration to above 2×10^4 cm^{-3}. The AgI-seeded case showed identifiable ice-crystal signatures together with a rapid decrease in liquid-droplet concentration. The total droplet concentration reached a short-lived peak of approximately 2.1×10^3 cm^{-3} and decreased to less than one-third of this peak within about 1 min, while droplets larger than 10 μm were strongly reduced within about 2 min. These representative experiments show that the chamber system can support controlled observations of aerosol, droplet, and ice-particle responses associated with warm-cloud and cold-cloud seeding materials.

1 Introduction

Aerosol–cloud–precipitation interactions are a fundamental but complex component of weather and cloud evolution, with important implications for radiative balance, regional hydrology, and weather-modification applications (Andreae and

https://doi.org/10.5194/egusphere-2026-3404
Preprint. Discussion started: 10 July 2026

Rosenfeld, 2008). Changes in aerosol loading can influence droplet activation, condensational growth, collision–coalescence, ice nucleation, cloud-phase partitioning, and precipitation formation, and may also affect cloud radiative properties through changes in cloud microphysical state (Chen et al., 2011; Morrison et al., 2020; Wang et al., 2026). Artificial weather modification aims to alter cloud microphysical processes through the introduction of seeding aerosols or seeding materials. However, cloud responses to seeding depend strongly on aerosol properties, thermodynamic conditions, cloud dynamics, and the background aerosol population, which makes the isolation and quantification of seeding effects difficult in natural clouds. Numerical modelling and field studies have provided important insight into how hygroscopic or glaciogenic seeding may modify cloud microphysical structure and precipitation development. Hybrid cloud microphysical models, large-eddy simulations, and other numerical frameworks have been used to examine the effects of hygroscopic particles on warm-rain formation, mixed-phase microphysics, ice-formation pathways, and precipitation-enhancement feasibility (Kuba and Murakami, 2010; Tonttila et al., 2022; Kuo et al., 2024; Lüttmer et al., 2025). Complementary field observations and evaluation studies have examined cloud responses to seeding under natural conditions and have emphasized the difficulty of separating seeding-induced signals from cloud evolution and meteorological variability (Li et al., 2022; Wu et al., 2018; Al Hosari et al., 2021; Gayatri et al., 2023). Field studies have also used microphysical diagnostics, such as changes in drop size distributions or coalescence-related indicators, to evaluate hygroscopic seeding responses (Tessendorf et al., 2021; Padmakumari et al., 2024). Verification approaches based on precipitation chemistry have further been proposed for assessing field seeding effects (Koo et al., 2025). These studies provide important scientific context, but field and model-based assessments still require controlled laboratory constraints on aerosol–cloud microphysical responses. Outcome-based evaluations, such as hydrological or agricultural impact assessments, are useful for operational programmes but cannot by themselves isolate chamber-scale microphysical mechanisms (Knowles and Skidmore, 2021).

Cloud chamber experiments offer a complementary means of investigating aerosol–cloud interactions and seeding responses under controlled and repeatable laboratory conditions. Adiabatic-expansion chambers are commonly used to simulate rapid cooling and supersaturation during cloud formation (Tajiri et al., 2013; Su et al., 2019). AIDA has been widely used to investigate aerosol phase transitions, ice nucleation, and ice-formation processes under controlled thermodynamic conditions (Wagner et al., 2011; Schnaiter et al., 2016). CERN CLOUD has advanced understanding of aerosol nucleation and growth in an ultra-clean and highly controlled chamber environment, with recent studies addressing atmospheric new-particle formation, biogenic particle formation, and upper-tropospheric isoprene-derived particles (Kirkby et al., 2023; Dada et al., 2023; Shen et al., 2024). The performance of large cloud chambers also depends on careful characterization of chamber conditions, including temperature uniformity and contamination control (Dias et al., 2017; Schnitzhofer et al., 2013). The Π chamber has been used to investigate turbulence effects on droplet growth and droplet-size spectral broadening, as well as turbulent mixing and microphysical uniformity in convection-cloud chamber simulations (Chang et al., 2016; Chandrakar et al., 2016; Thomas et al., 2023; Thomas et al., 2025). More recently, K-CPEC has been developed for controlled cloud-physics and weather-modification studies, including the characterization of hygroscopic seeding materials under chamber conditions (Park et al., 2025; Kim et al., 2025). These developments show that cloud chamber research is increasingly moving towards integrated

https://doi.org/10.5194/egusphere-2026-3404
Preprint. Discussion started: 10 July 2026

instrumentation, controlled thermodynamic forcing, and closer links between laboratory measurements, microphysical modelling, and weather-modification applications (Shaw et al., 2025).

Seeding-material research remains central to artificial weather modification. For warm-cloud applications, hygroscopic materials such as salts and modified salt formulations can influence droplet activation and growth by altering the population of particles available for water-vapour uptake (Silverman and Sukarnjanaset, 2000; Silverman, 2003; Rosenfeld et al., 2010; Wang et al., 2019). Related experimental and theoretical studies have also examined the modification of warm fog by salty drops, illustrating the broader role of hygroscopic particles in liquid-cloud and fog microphysical evolution (Khain et al., 2024). Chamber-based studies have begun to characterize seeding materials more directly. MRI cloud chamber experiments evaluated both cloud condensation nuclei and ice-nucleating abilities of seeding materials, including salt micro-powders, hygroscopic flares, and AgI-based particles (Tajiri et al., 2015). More recently, Kim et al. (2025) used K-CPEC to analyse the particle characteristics and cloud-droplet growth properties of powder-type NaCl and $CaCl_2$ seeding materials. For cold-cloud applications, laboratory studies of AgI-type aerosols have provided important constraints on ice-nucleation mechanisms and the behaviour of artificial ice-nucleating particles in simulated cloud environments (Mossop, 1969; DeMott, 1995). Reviews and recent studies have further highlighted the importance of ice-nucleating particle properties, ice-crystal growth, and cloud-phase conversion in glaciogenic seeding processes (Murray et al., 2012; Miller et al., 2025; Fuchs et al., 2025).

Despite these advances, laboratory evidence remains limited on how the introduction of seeding materials modifies aerosol, droplet, and ice-particle populations under controlled conditions, especially within a single framework applicable to both warm-cloud and cold-cloud experiments. Field studies are influenced by natural cloud variability, changes in background aerosol loading, and meteorological uncertainty, whereas numerical studies require laboratory observations to constrain key microphysical responses. A reproducible chamber platform with controlled thermodynamic forcing and integrated particle measurements is therefore needed for paired background–seeded comparisons.

In this study, we developed a cloud chamber system that controls temperature, pressure, and humidity and measures particles across the aerosol, cloud-droplet, and ice-particle size ranges. We characterize the chamber performance in terms of thermal, pressure, and humidity control. We then demonstrate its application through representative paired experiments involving hygroscopic powder seeding under warm-cloud conditions and AgI seeding under cold-cloud conditions.

2 Experimental Equipment

2.1 Cloud Chamber Structure

The cloud chamber system consists of two cylindrical stainless-steel vessels, denoted chamber A (2.7 ± 1 % m^3) and chambe r B (9.0 ± 1 % m^3) (Fig. 1). Chamber A is 1.2 m in diameter and 2.4 m in height, whereas chamber B is 1.8 m in diameter and 3.6 m in height (Table 1). Both chambers have smooth inner walls to reduce condensation losses and are equipped with optic al windows for direct observation of cloud and particle evolution. The two chambers can operate either independently or in a differential-pressure configuration. They are interconnected by three electrically actuated valves, their open–closed state and

https://doi.org/10.5194/egusphere-2026-3404
Preprint. Discussion started: 10 July 2026

valve opening can be controlled independently by the control system. In independent mode, the connecting valves remain closed and each chamber is used separately for cloud-chamber experiments or expansion-induced cloud formation. In differential-pressure mode, one chamber can first be evacuated below ambient pressure, and the resulting pressure difference can then be used to regulate the expansion rate and pressure drop in the main experimental chamber by controlling the number of open valves and the valve opening. Both chambers are connected to a common pressure-control and vacuum system. A mechanical vacuum pump (GLWZ-50; nominal pumping speed: 50 L s^{-1}) is installed at the base of the system and connected to the chambers through a 50 mm inlet line and a 40 mm exhaust line. In addition, each chamber is equipped with a controllable bottom valve connected to the ambient environment. After evacuation or expansion experiments, this valve is opened to allow outside air to re-enter the chamber and restore near-ambient pressure. Fig. 1a also shows the main auxiliary subsystems. The humidity-control system is connected to the chambers through dedicated inlet lines. Powder catalysts are introduced through a top-mounted catalyst-spreading device. For flame-based cold-cloud experiments, an independent combustion chamber is connected to an air-mixing chamber, and the resulting catalyst-laden flow is introduced into the main chamber through a dedicated seeding line.

A controlled pressure drop causes the enclosed air to expand and cool nearly adiabatically. Over this short timescale, the water-vapor mixing ratio changes little prior to the onset of condensation, whereas the temperature decreases rapidly. The resulting decrease in saturation vapor pressure drives the relative humidity upward, and once supersaturation is reached, water vapor condenses onto available aerosol particles or seeded nuclei to form cloud droplets. In this way, the system reproduces the essential thermodynamic pathway of atmospheric cloud formation, in which expansion cooling of rising air leads to supersaturation and subsequent condensation. All cloud-formation, seeding, and performance tests reported in this study were conducted in chamber B only, while the connecting valves between chambers A and B remained closed throughout. Under this operating mode, rapid pressure reduction in chamber B leads to adiabatic expansion and cooling, thereby generating supersaturation and initiating cloud or fog formation. The cloud chamber combines adjustable temperature, pressure, and humidity control with integrated measurements of aerosols, droplets, and ice particles

https://doi.org/10.5194/egusphere-2026-3404
Preprint. Discussion started: 10 July 2026

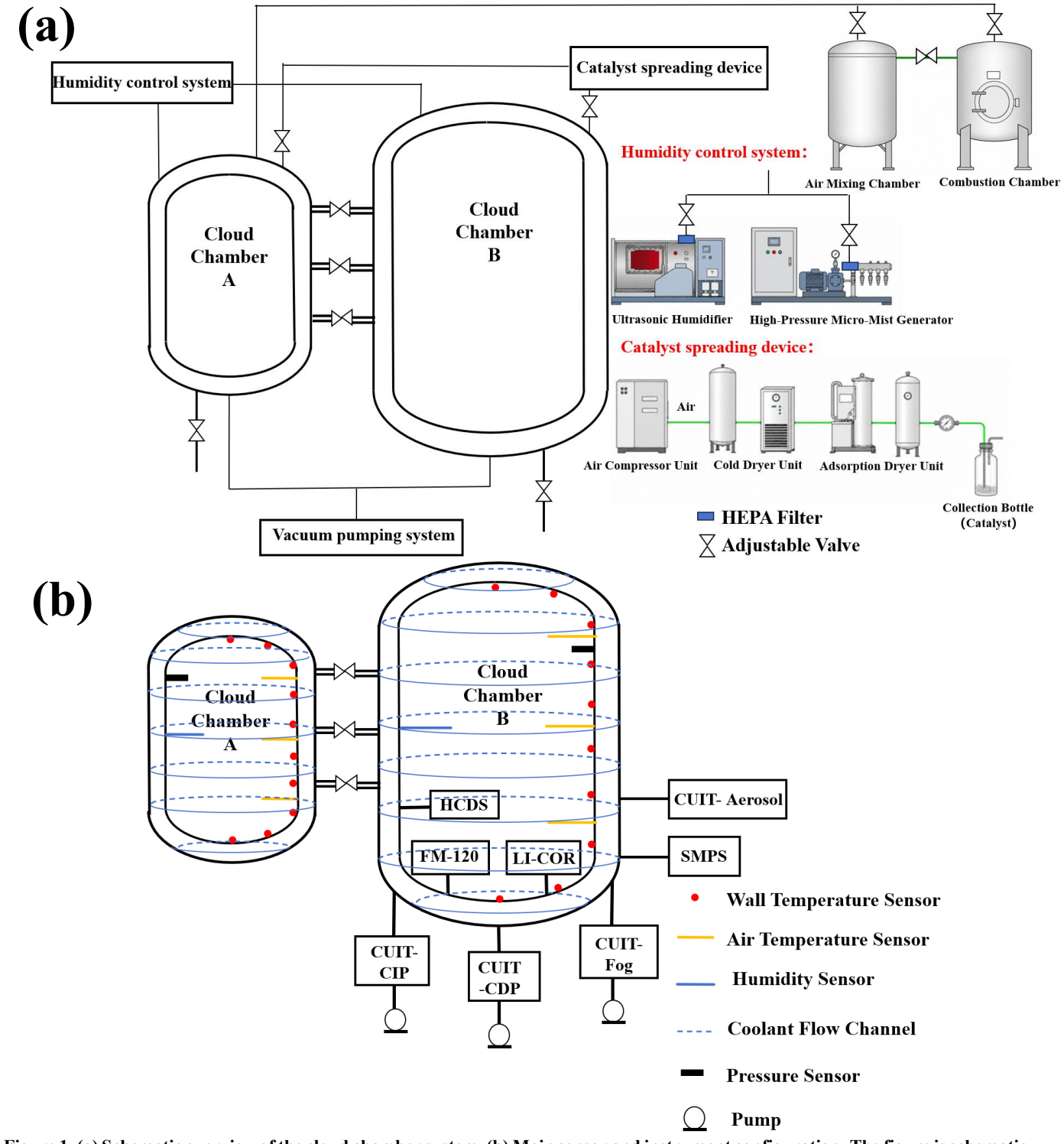

Figure 1. (a) Schematic overview of the cloud chamber system. (b) Main sensor and instrument configuration. The figure is schematic and not to scale.

https://doi.org/10.5194/egusphere-2026-3404
Preprint. Discussion started: 10 July 2026

Table 1. Main Structural Parameters Of The Cloud Chamber.

Type	Dimensions	Volume	Pressure/Temperature	Materials
Cloud chamber A	Diameter 1.2 m, Height 2.4 m	2.7 m³ (±1 %)	30-1100 hPa/ -40-40 °C	316 L stainless steel
Cloud chamber B	Diameter 1.8 m, Height 3.6 m	9 m³ (±1 %)		

The cloud chamber is equipped with a comprehensive suite of instruments designed to monitor the microphysical properties of aerosols, cloud droplets (Table 2). The key instruments included several probes independently developed at Chengdu University of Information Technology (CUIT), namely the CUIT-Aerosol atmospheric aerosol size spectrometer, the CUIT-Fog fog monitor, the CUIT-CDP cloud droplet probe, and the CUIT-CIP cloud imaging probe. Additional instruments included a fog monitor (FM-120), a LI-COR 7500DS gas analyzer, and a holographic cloud droplet spectrometer. The main instruments used in the cloud chamber and their measurement principles are summarized in Table 2. The FM-120, LI-COR 7500DS, and holographic cloud droplet spectrometer (HCDS) were installed inside chamber B near the bottom for in situ measurements. In contrast, the CUIT-CIP, CUIT-CDP, and CUIT-Fog were located outside the chamber base and connected to the lower part of chamber B through short dedicated sampling lines. The sampling lines were approximately 100 mm long; the CUIT-Fog and CUIT-CDP used two separate lines with an inner diameter of 16 mm, whereas the CUIT-CIP used a larger line with an inner diameter of 40 mm. Each of these three instruments used an independent sampling pump to draw chamber air for measurement. The CUIT-Aerosol and SMPS were also operated as external sampling-based instruments for aerosol measurements. To minimize droplet-settling losses, adjustable valves and a variable-frequency vacuum pump were used to control the sampling flow rate and total sampled volume, thereby ensuring that the collected samples were representative of the cloud or fog field. A Bipolar scanning mobility particle sizer (SMPS), consisting of a soft X-ray neutralizer (homemade), a long differential mobility analyzer (DMA; homemade), and a butanol-based condensation particle counter (CPC-W003; homemade), was used to measure submicron aerosol particle-size distributions. A POPS optical particle spectrometer (Nanjing Handix Environmental Technology Co.) was used for aerosol intercomparison and calibration only and was not part of the in-chamber measurement system during the cloud experiments. Together, the instruments used in the chamber provided continuous measurement coverage from aerosols to cloud and precipitation particles, enabling real-time characterization of particle-size distributions, number concentrations, and particle morphology. During the experiments, the CUIT-Aerosol was used to monitor aerosol number concentration and size distribution before and after expansion, whereas the FM-120 fog monitor and the cloud droplet probe were used to measure droplet size distributions. The CUIT-CIP and the holographic cloud droplet spectrometer were used to characterize the morphology and temporal evolution of larger droplets and ice crystals. To ensure measurement accuracy and inter-instrument consistency, Fig. 2a shows the calibration results of the SMPS, POPS, and CUIT-Aerosol.

https://doi.org/10.5194/egusphere-2026-3404
Preprint. Discussion started: 10 July 2026

150

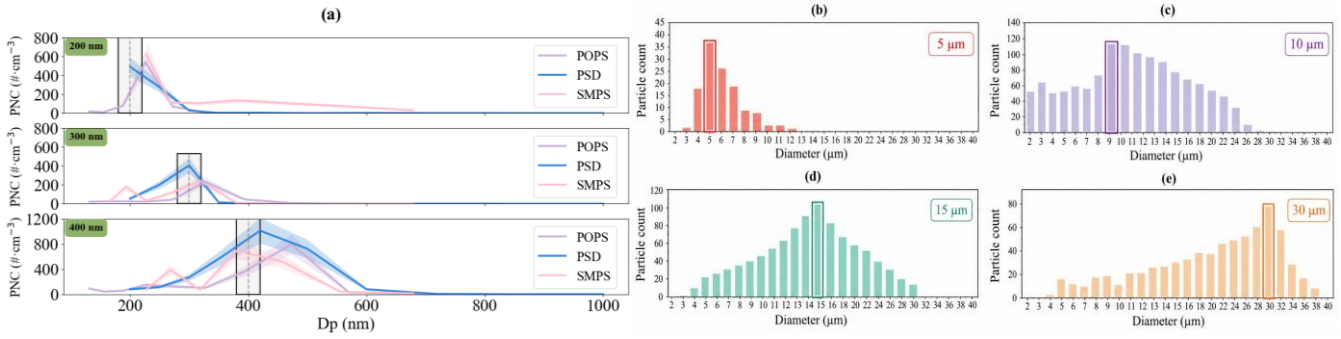

Figure 2. (a) Calibration of particle size distribution intercomparison among the CUIT-Aerosol, SMPS, and POPS for 200, 300, and 400 nm standard nanoparticles. (b–e) Calibration using 5, 10, 15, and 30 μm standard particles of CUIT-CDP.

Specialized illumination and imaging systems are incorporated to enable detailed visualization of cloud droplets and particles. The lighting system consists of cryogenic-resistant LED arrays uniformly distributed along the chamber's curved top and side walls. It offers adjustable brightness from 0 to 20000 lux /5000 K, accommodating diverse imaging requirements. A high-intensity pulsed laser positioned at the top of the chamber, synchronized with a high-speed camera, enables droplet scattering imaging. The imaging system features a high-resolution digital camera and a high-speed camera, both designed to operate reliably under cryogenic conditions. The high-speed camera achieves frame rates over 600 fps at 1280 × 1024 resolution, with faster speeds available at lower resolutions, facilitating the capture of rapid cloud droplet evolution. When synchronized with the pulsed laser, the system records real-time images of condensed cloud droplets right after the expansion.

https://doi.org/10.5194/egusphere-2026-3404
Preprint. Discussion started: 10 July 2026

Table 2. Cloud Chamber Measuring Instruments.

Parameter	Manufacture	Sampling flow rate	Range	Sampling period	Measurement principle
Atmospheric aerosol size spectrometer	(CUIT- Aerosol)	0.2-20 $m \cdot s^{-1}$	0.2-40 μm	1 s	Optical particle detection
Scanning Mobility Particle Sizer	(SMPS)	1 $L \cdot min^{-1}$	7.4-286 nm	5 min	Electrical mobility classification combined with condensation particle counting
Fog monitor	(FM-120; DMT) (CUIT-Fog)	1 $L \cdot min^{-1}$/15 $m \cdot s^{-1}$	2-50 μm	1-10 s	Single-particle forward light scattering
Cloud Droplet Probe	(CUIT-CDP)	2-10 $m \cdot s^{-1}$	2-50 μm	1-10 s	Laser forward scattering with depth-of-field qualification
Cloud Imaging Probe	(CUIT-CIP)	5 $L \cdot min^{-1}$	25-1550 μm	1-10 s	Optical array imaging
CO_2/H_2O analyzer	(LI-COR 7500DS)	N/A	0-60 mmol	30 Hz	Non-dispersive infrared absorption (NDIR)
Holographic Cloud Droplet Spectrometer	(HCDS)	N/A	2-50 μm	150 Hz	Digital in-line holography
Pressure	(YK-1006,Jining Shenyang Vacuum Instrument Co)	N/A	10-1100 hPa	1 s	N/A
Temperature	(PT-100, Wuxi Zhongce Sensor Technology Co)	N/A	-60-160 °C	1 s	N/A
Humidity	(KYWS-SX, Beijing Kunlun Coast Instrument Technology Co)	N/A	0-100% RH	1 s	N/A

2.2 Cloud Chamber Environment Control System

The cloud chamber system is equipped with an integrated temperature control and monitoring system. Before conducting low-temperature experiments, such as cold-cloud formation, the chambers are pre-cooled. Thermal regulation is provided by a two-stage vapor-compression refrigeration system consisting of a chiller unit, circulation pumps, and a cooling tower. During operation, the secondary coolant is first cooled by the chiller and then circulated through the chamber-wall cooling circuits, which remove heat from the vessel walls, thereby lowering the temperature of the gas inside the chambers. Both chambers A and B employ a double-layer jacketed cooling configuration with secondary-coolant flow channels. The jacket is divided into multiple vertical layers, each with independent coolant inlets and outlets, enabling stratified thermal regulation. Absolute ethanol is used as the secondary coolant. Chamber B is equipped with nine circulation channels, while chamber A has seven.

https://doi.org/10.5194/egusphere-2026-3404
Preprint. Discussion started: 10 July 2026

Each channel is fitted with an independent valve, pressure regulator (YK-1006), and flowmeter (PGLWGY-DN20). The coolant flow in each branch can be controlled by adjusting the pump frequency, ensuring uniform wall cooling.

The system provides zonal thermal control in a 6+1 configuration, consisting of six primary circuits and one bypass loop. Real-time temperature and humidity monitoring is performed using PT-100 platinum resistance thermometers (±0.1°C), thermocouples, and a KYWS-SX humidity meter. Based on sensor feedback, the system performs zonal temperature regulation and real-time monitoring and control of chamber humidity. In addition, proportional valves regulate the secondary-coolant flow in each branch to maintain a uniform and stable chamber temperature field. Tests confirmed that both chambers A and B can be stably controlled over a temperature range of -40 to 40 °C.

In chamber B, three temperature-control experiments were conducted to evaluate the thermal performance of the system. In the upper-temperature limit test (Fig. 3a), the initial temperatures in the upper, middle, and lower sections of the chamber were all around 26 °C. Following a 30-minute heating phase, the temperature stabilized at 40 °C for 15 minutes, resulting in an average heating rate of 0.47 °C min^{-1}. During the lower-limit temperature test (Fig. 3c), the chamber temperature gradually dropped from approximately 26 °C to -40 °C over 300 minutes, corresponding to an average cooling rate of 0.216 °C min^{-1}. For the temperature-gradient test (Fig. 3b), the chamber was first stabilized at 0°C (± 0.5 °C) for approximately 102 minutes, then gradually cooled from 0 °C to -10 °C over the next 110 minutes. The temperature was held at −10 °C (± 0.5 °C) for about 4 minutes before a controlled descent to -20 °C, which occurred over a 189-minute period. The final temperature of -20 °C (± 0.5 °C) was sustained for approximately 30 minutes. Across all three low-temperature plateaus (-20 °C, -10 °C, and 0 °C), the system quickly reached steady-state conditions, with fluctuations confined within ±0.5 °C and vertical temperature differences among the upper, middle, and lower layers remaining below 0.3 °C. During the heating and cooling cycles, the vertical temperature profile remained stable, with inter-layer differences within 1 °C, demonstrating the system's strong thermal stability.

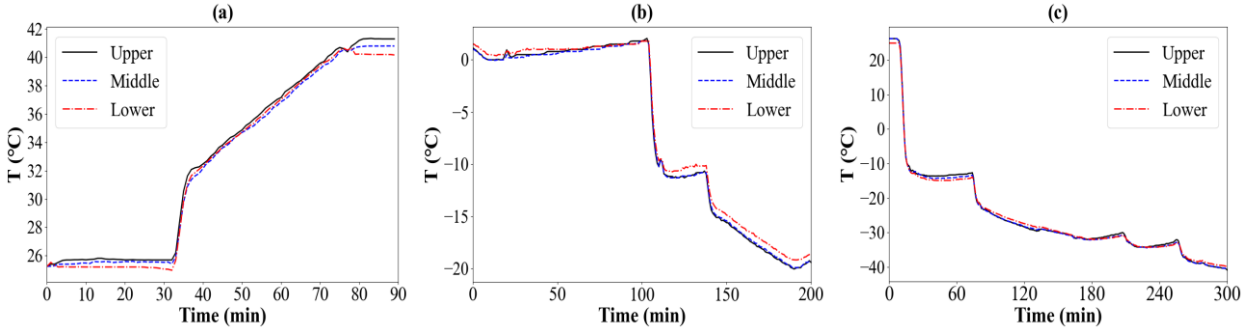

Figure 3. Temperature-control tests conducted in chamber B: (a) top temperature limit test, (b) temperature gradient test, (c) bottom temperature limit test.

Fig. 4a and 4b show the temperature stability in chamber B. The temperatures in the upper (3 m), middle (2 m), and lower (1 m) layers, as well as that at the tenth wall layer, remained within 15.0–16.0 °C. The temperature difference between adjacent

https://doi.org/10.5194/egusphere-2026-3404
Preprint. Discussion started: 10 July 2026

layers remained within 1 °C. Air temperature sensors are placed at heights of 1 m, 2 m, and 3 m above the chamber floor, and ten wall temperature sensors are evenly distributed along the chamber walls. While occasional minor fluctuations were observed, the vertical temperature profile remained stable, reflecting excellent thermal uniformity across the chamber. The chamber uses a multi-layer temperature-control system in which wall temperatures are regulated through heat exchange with a circulating secondary coolant. The thermal inertia of the stainless-steel chamber walls helps maintain gradual and stable temperature changes, thereby supporting a uniform thermal environment. This sensor configuration allows real-time monitoring and precise control of both the vertical and radial temperature structure during the experiments.

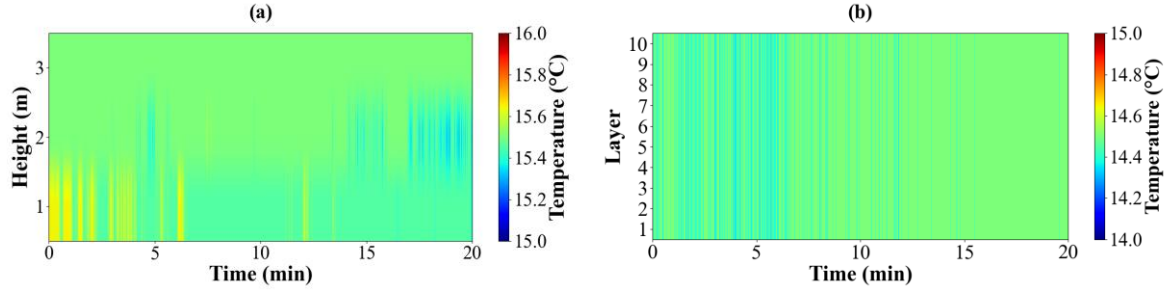

Figure 4. Wall Temperature stability in chamber B: (a) air-temperature stability test and (b) ten-layer wall-temperature stability test.

The pressure control system of the cloud chamber consists of four primary components: a vacuum pump unit, an air compressor unit, a buffer tank, and a valve array. The system regulates chamber pressure within a range of 30 to 1100 hPa, supporting experiments under both sub-atmospheric and super-atmospheric conditions. Efficient and stable vacuum operation is maintained even at temperatures as low as -40 °C through the use of horizontal screw vacuum pumps equipped with integrated heat-exchange mechanisms. Pressure sensors within the chamber monitor pressure variations in real time and capture transient pressure curves during expansion events. The integrated control system can regulate the expansion rate over a broad range, from several hundred to several thousand pascals per minute depending on the valve settings and experimental protocol, thereby simulating the adiabatic cooling dynamics typical of atmospheric updrafts at varying intensities.

Fig. 5 presents the results of the pressure limit and relative humidity test in chamber B. During pressurization, the chamber pressure increased from ambient to 1100 hPa in about two minutes, at an average rate of 117.44 $hPa \cdot min^{-1}$. After returning to and stabilizing at atmospheric pressure, the system initiated decompression, reducing the pressure to 30 hPa over a period of about 13 minutes, with an average rate of 72.60 $hPa \cdot min^{-1}$. The chamber then remained in a very low-pressure state for about 1-2 min before gradual venting was initiated. Overall, the system successfully completed a full pressure cycle between 30 and 1100 hPa, demonstrating stability and responsiveness.

The implementation of an integrated vapor regulation system ensures precise control of the initial humidity parameters required for specific experimental protocols. The system integrates an ultrasonic humidifier, a high-pressure micro-mist generator, a variable-frequency blower fan, and a high-efficiency air filter to provide comprehensive humidity conditioning. The ultrasonic

https://doi.org/10.5194/egusphere-2026-3404
Preprint. Discussion started: 10 July 2026

humidifier generates ultrafine pure-water droplets (1-10 μm) that are delivered into the chamber through pipelines to promote vapor dispersion, whereas the high-pressure micro-mist generator pressurizes pure water to 1-3 MPa and injects fine droplets through chamber nozzles for rapid humidification and internal spray cleaning. Chamber humidification is achieved either by drawing in saturated vapor through pressure differentials generated during evacuation or by injecting atomized moisture with the aid of the internal blower fan. To ensure air purity, all air inlets are equipped with HEPA-grade filters. The vapor delivery rate is finely controlled by modulating the blower fan speed. These conditioning mechanisms establish a near-saturated initial state, ensuring the desired supersaturation during subsequent expansion processes. Compressed air, treated by a dry-air module, is introduced into the chamber to remove residual moisture, facilitating rapid humidity reduction and efficient drying. In Fig. 5, the relative humidity decreased from approximately 98.4 % to 10.3 % within 15 minutes, followed by a re-humidification process that restored it to 96.8 % over the subsequent 20 minutes.

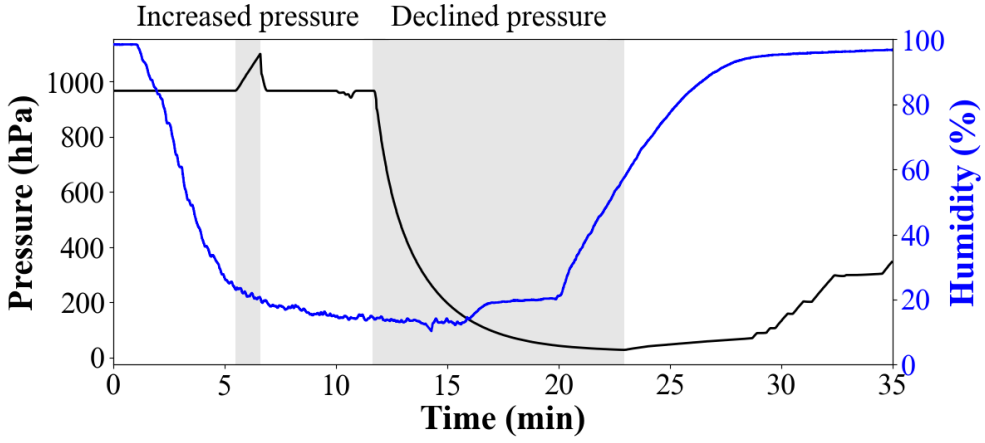

Figure 5. Pressure and relative humidity tests conducted in chamber B

In the present experiments, the chamber background was not generated from composition-controlled clean air. After each experiment, the chamber was returned to near-ambient pressure by opening the controllable bottom valve, allowing ambient air to re-enter the chamber. Therefore, the background aerosol was derived from ambient air under the environmental conditions at the time of each experiment. Within each paired comparison, the background and seeded cases were conducted consecutively within the same time window and were initialized from the same ambient aerosol source. This design reduces, but does not eliminate, the influence of short-term background-aerosol variability. Because residual particles, wall effects, and changes in ambient aerosol loading may still affect the measurements, the seeded-background differences are interpreted as chamber-scale microphysical responses under closely matched ambient-aerosol conditions. The cases shown below are representative paired background-seeded experiments with concurrent measurements of pressure, temperature, relative humidity, and particle size distributions.

https://doi.org/10.5194/egusphere-2026-3404
Preprint. Discussion started: 10 July 2026

3 Representative Warm-Cloud Seeding Experiment

The cloud chamber is designed with two separate dispersion systems to simulate the diffusion and interaction of various catalyst types in cloud environments: one for powder-based catalysts and another for flame-based catalysts.

Powder catalysts are delivered using a top-down method with two distinct techniques. In the first method, compressed air was pressurized to 0.8 MPa and dried to generate a stable carrier airflow with a flow rate of 1.17 m^3/min. The airflow rate was manually adjusted using a flowmeter to achieve the desired delivery velocity. The powder catalyst, primarily composed of $CaCl_2$, plant ash, and composite materials, was loaded into a collection bottle fitted with a long inlet tube and a short outlet tube. Once the valve at the top of the chamber was opened, the dried airflow entered the bottle through the long inlet, entraining the powder catalyst, and carried it through the short outlet into the chamber. This method introduced the catalyst from the top of the chamber, dispersing it downward. The hygroscopic catalyst promotes droplet growth by enhancing condensation and accelerating cloud formation. The second method employed an RBG dry powder aerosol generator, which was connected directly to the inlet at the top of the chamber. In this system, the powder was first loaded into a cylindrical reservoir and then conveyed upward at a controlled feed rate to a rotating brush. A high-velocity dispersing airflow generated within the instrument removed the powder from the brush and dispersed it in the dispersion head, thereby introducing the particles into the chamber from the top. For expansion-driven cloud formation experiments, the first configuration is usually preferred, as it offers better control over both dispersion dynamics and catalyst-cloud interactions.

In the warm-cloud seeding experiment (Fig. 7), the background case was established without introducing any additional seeding agent or standard aerosol. As described above, both the background and catalyzed cases within each paired experiment were initialized from the same ambient aerosol source. Under this background condition, warm-cloud formation in chamber B was initiated by rapid pressure reduction, which induced adiabatic expansion and cooling and thereby generated a supersaturated environment. Subsequently, 10 g of hygroscopic seeding powder was released from the top of the chamber 10 s after cloud formation began in order to compare the microphysical evolution before and after seeding. Fig. 6 Sequential images of warm-cloud formation in chamber B at (a) the onset of cloud formation, (b) 10 s, and (c) 30 s after cloud formation. After cloud formation, widespread cloud and fog developed throughout the chamber, resulting in a clear reduction in visibility relative to the pre-formation state.

https://doi.org/10.5194/egusphere-2026-3404
Preprint. Discussion started: 10 July 2026

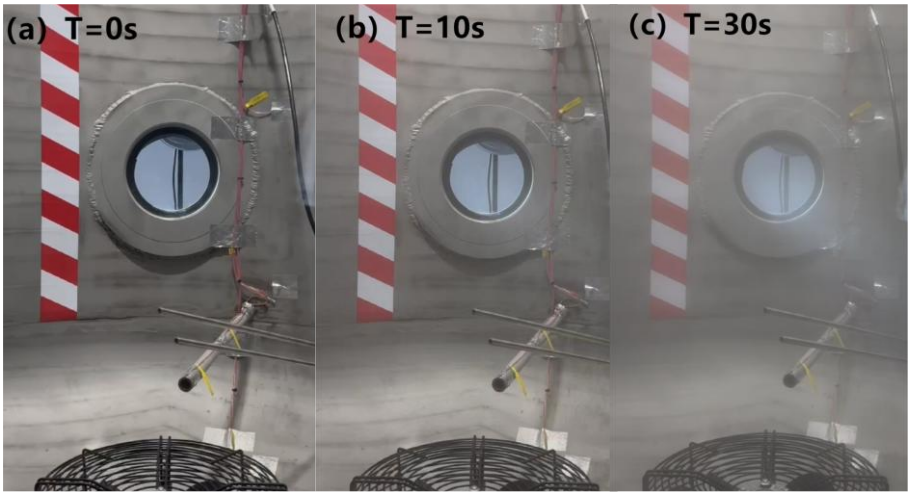

Figure 6. Images of warm-cloud formation in chamber B

Fig. 7a-b illustrate that during the background experiment, aerosol particle sizes were mostly in the 0.2-0.7 µm range, with total number concentrations below about 2000 #·cm^{-3}. In contrast, the aerosol number concentration spiked within 10 seconds of cloud formation during the catalytic experiment. Distinct peaks were observed at approximately 0.3 µm, 0.7 µm, and 1.5 µm, with the 0.3 µm peak surpassing 3000 #·cm^{-3}, a significant increase compared to the background case. This indicates that catalyst release increased the number of particles available for droplet formation.

Fig. 7c-d show the fog droplet size distributions. During the background experiment, the droplet sizes steadily increased, with the majority of droplets ranging between 3 and 10 µm. The average concentration of droplets exceeding 12 µm reached 1357 #·cm^{-3}. Larger droplets then formed through collision-coalescence and condensational growth as vapor condensation continued. In this case, the efficiency of cloud formation was constrained by the availability of ambient aerosol particles, which served as condensation nuclei. The introduction of hygroscopic seeding powder was followed by a rapid increase in 3-10 µm droplet concentrations, with a pronounced peak during the first 0-2 min. However, droplets ≥12 µm were less abundant in the seeded case than in the background case, with the average concentration decreasing from 1357 to 478 cm^{-3}. This response suggests that the introduced hygroscopic particles enhanced water-vapour competition and favoured the rapid formation of numerous small droplets, rather than sustained growth of larger droplets. Gravitational settling and shorter cloud persistence have contributed to the reduced large-droplet concentration. Fig. 7e-f show the pressure, temperature, and relative-humidity evolution during the paired warm-cloud background and hygroscopic-seeding experiments. In both cases, pressure reduction and the accompanying temperature decrease indicate expansion-induced cloud formation. The average pressure-drop rates were 26.84 hPa min^{-1} in the background case and 27.72 hPa min^{-1} in the seeded case, and the corresponding cooling rates were 0.49 and 0.61 °C min^{-1}, respectively. The RH decrease rate was higher in the seeded case than in the background case, increasing from 0.47 to 0.75 %RH min^{-1}. This stronger RH decrease is consistent with enhanced water-vapour consumption after the introduction of hygroscopic particles. The enhanced vapour competition likely favoured the rapid formation of small droplets while limiting the sustained growth of larger droplets.

https://doi.org/10.5194/egusphere-2026-3404
Preprint. Discussion started: 10 July 2026

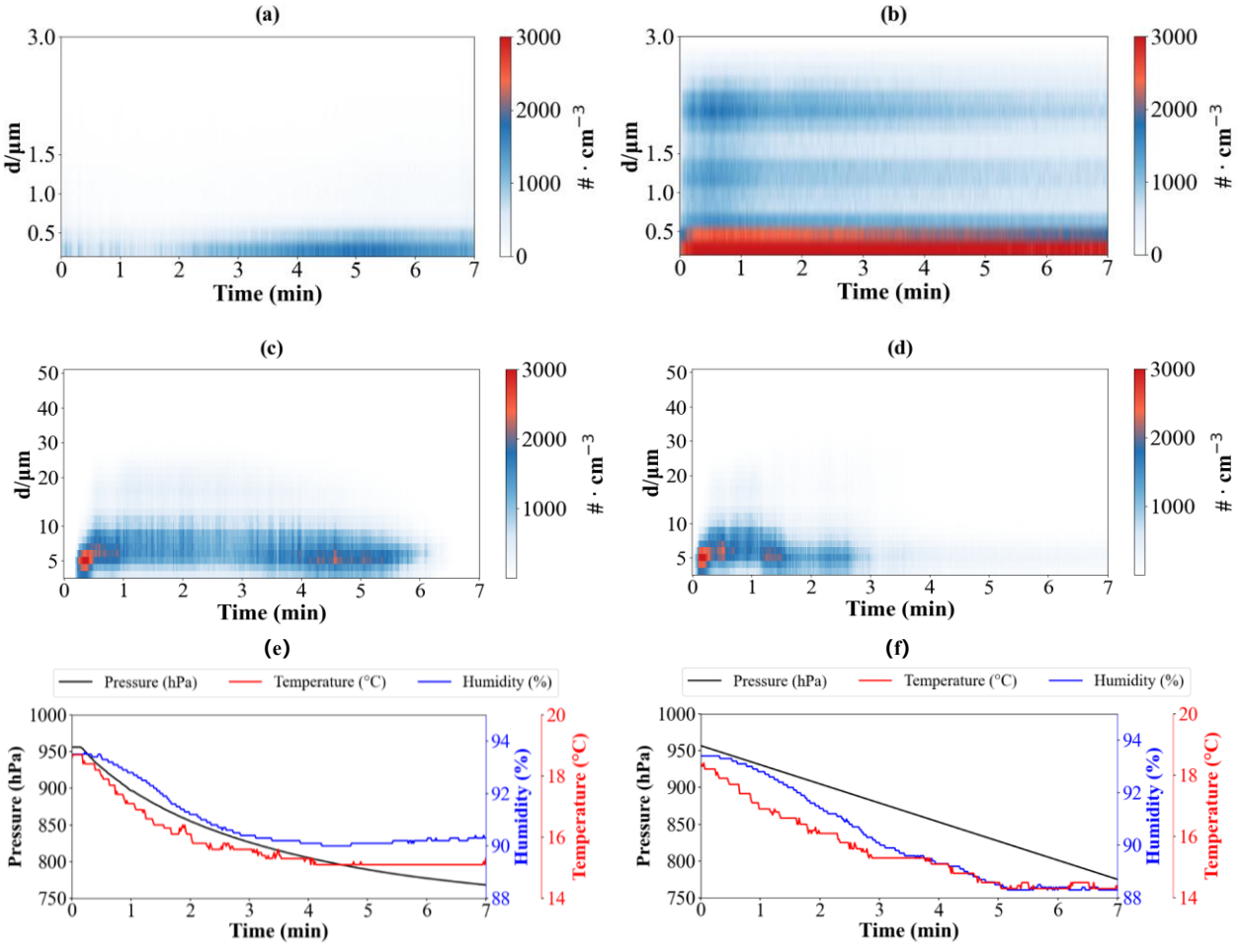

Figure 7. Results of the paired warm-cloud background and hygroscopic-seeding experiments. (a, b) Time-resolved aerosol number concentrations in the background and seeded cases, respectively. (c, d) Corresponding droplet size distributions. (e, f) Pressure, temperature, and relative humidity during the background and seeded cases, respectively.

4 Representative Cold-Cloud AgI Seeding Experiment

The flame-catalyst dispersion system consists of an independent combustion chamber, a mixing/dilution tank, and a connected pipeline network. Before each experiment, flame catalysts (e.g., silver iodide smoke sticks) were ignited in the combustion chamber, producing high-temperature combustion products with active nucleating species. When high concentrations of combustion particulates were generated, the mixing/dilution tank mixed the exhaust with compressed air to control dilution, optimizing aerosol concentrations for instrument detection and experimental needs. A vacuum pump was used to extract gas from the cloud chamber, generating a slight negative pressure inside the tank. The pump and valves were then closed. Opening

https://doi.org/10.5194/egusphere-2026-3404
Preprint. Discussion started: 10 July 2026

the valve between the combustion or dilution tank and the chamber allowed the combustion products to enter the chamber rapidly under the imposed pressure gradient. During the process, the aerosol size spectrometer continuously tracked both the concentration and size distribution of aerosols within the chamber. When the aerosol concentration exceeded the predefined threshold, the valves were promptly closed to stop catalyst input, thereby maintaining controlled experimental conditions.

In the cold-cloud seeding experiment (Fig. 9), chamber B was precooled to -4 °C by the refrigeration system. The background case was conducted without introducing any additional seeding agent or standard aerosol. As described above, both the background and seeded cases within each paired experiment were initialized from the same ambient aerosol source. Under this background condition, cold-cloud formation was initiated by rapid pressure reduction, which induced adiabatic expansion and cooling. During the AgI-seeded case at -4 °C, 0.5 g of AgI was ignited, and the resulting AgI combustion aerosol was introduced into chamber B at 16:41. As shown in the HCDS images in Fig. 8, no identifiable ice-crystal signatures were observed in the unseeded case (Fig. 8a), whereas particles with identifiable ice-crystal signatures were observed after the introduction of AgI in the AgI-seeded case (Fig. 8b). These ice-crystal-like signatures were identified mainly from their non-spherical morphology and optical appearance relative to nearly spherical liquid droplets in the HCDS images.

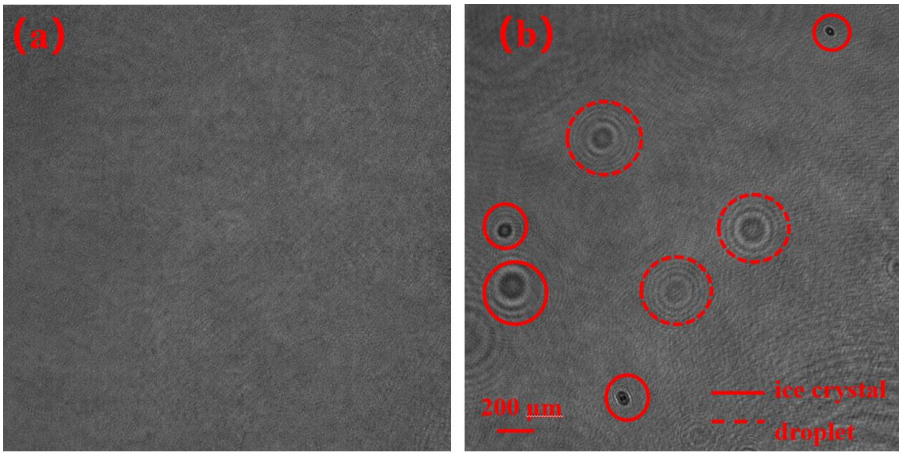

Figure 8. HCDS images from the paired cold-cloud experiments. (a) Unseeded after 1 min. (b) AgI-seeded after 1 min.

Fig. 9a-b show the aerosol particle size distributions. In the background experiment, aerosol particles were mostly concentrated in the 0.6-1.4 μm range, with total number concentrations ranging from 5000 to 10000 #·cm^{-3}. After introducing AgI, the number concentration of particles in the 0.3-0.7 μm range quickly rose above 20000 #·cm^{-3} and stayed elevated throughout cloud formation. These results indicate that AgI substantially enhanced the population of submicron aerosol particles within the chamber.

The droplet size distributions are presented in Fig. 9c-d. In the background experiment, most droplets were distributed within the 5-20 μm range, and high liquid-droplet concentrations were maintained throughout cloud formation. The total droplet concentration reached a peak of approximately 3.1 × 10^3 cm^{-3} and remained relatively high during the following several minutes, indicating a comparatively persistent liquid-cloud stage. In contrast, after the introduction of 0.5 g of AgI, small droplets in the 3–8 μm range increased rapidly immediately after cloud formation, with the total droplet concentration reaching

https://doi.org/10.5194/egusphere-2026-3404
Preprint. Discussion started: 10 July 2026

a short-lived peak of approximately 2.1×10^3 cm^{-3}. The concentration then decreased rapidly, falling to less than one-third of the peak value within about 1 min, and droplets larger than 10 μm were strongly reduced across the measured size bins within about 2 min. These observations are consistent with enhanced ice-phase development after the introduction of AgI-containing aerosol in the present chamber experiment. Possible contributing processes include droplet freezing, vapour competition between liquid droplets and ice particles, and the removal of larger ice or mixed-phase particles, which may have shortened the persistence of the liquid cloud. Overall, the paired droplet spectra suggest that the AgI-seeded case underwent a different microphysical evolution from the background case, with evidence of ice-phase processes rather than sustained liquid-droplet growth.

Fig. 9e-f show the pressure, temperature, relative humidity, and H_2O concentration evolution during the paired cold-cloud background and AgI-seeded experiments. In both cases, pressure reduction and the accompanying temperature decrease indicate expansion-induced cold-cloud formation. The average pressure-drop rates were 32.63 hPa min^{-1} in the background case and 32.91 hPa min^{-1} in the AgI-seeded case, and the corresponding cooling rates were 0.75 and 0.81 °C min^{-1}, respectively. The RH decrease rates were 1.63 and 1.46 %RH min^{-1} in the background and AgI-seeded cases, respectively. The measured H_2O concentration was further used to estimate the saturation ratios with respect to liquid water and ice, using saturation vapour pressures over liquid water and ice following Murphy and Koop (2005). The mean saturation ratios with respect to liquid water and ice were estimated to be S_w=0.942 and S_i=1.006 in the background case, indicating a cold-fog environment slightly below water saturation and close to ice saturation. In the AgI-seeded case, the corresponding mean values were higher, with S_w=1.222 and S_i=1.323, indicating stronger water- and ice-supersaturated conditions during the seeded experiment.

https://doi.org/10.5194/egusphere-2026-3404
Preprint. Discussion started: 10 July 2026

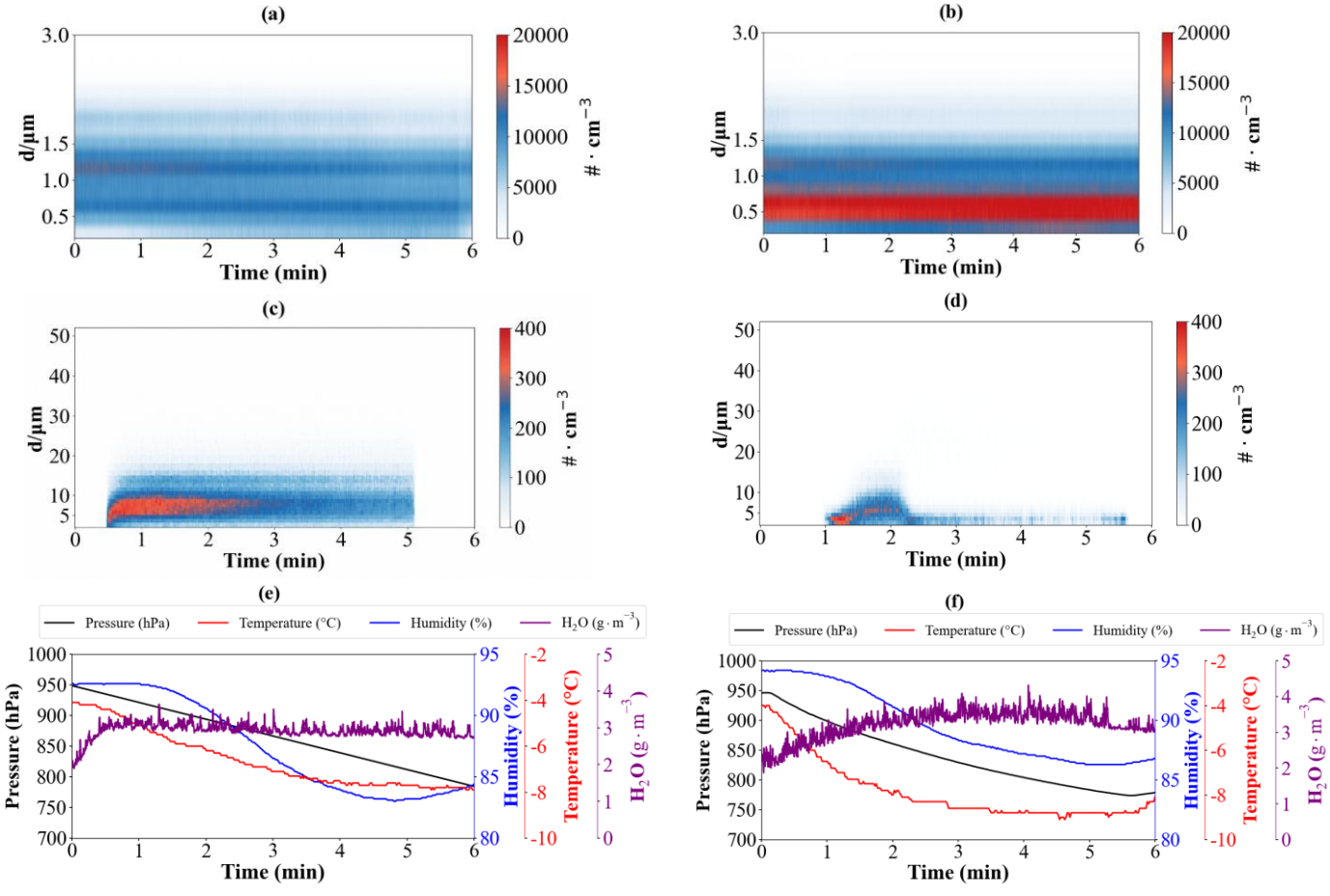

Figure 9. Results of the paired cold-cloud background and AgI-seeding experiments. (a, b) Time-resolved aerosol number concentrations in the background and AgI-seeded cases, respectively. (c, d) Corresponding droplet size distributions. (e, f) Pressure, temperature, relative humidity, and H_2O concentration during the background and AgI-seeded cases, respectively.

5 Conclusions and Discussion

The cloud chamber, which allows controlled adjustment of temperature, humidity, pressure, and water vapour, was used to conduct seeding experiments under both warm-cloud and cold-cloud conditions. By integrating measurements of thermodynamic variables with aerosol and droplet size distributions, we investigated cloud-formation characteristics and microphysical responses under different catalyst conditions. The chamber provides stable control of temperature (-40-40 °C) and pressure (30-1100 hPa), maintains small vertical temperature gradients, and allows independent adjustment of humidity and water-vapour conditions. The chamber was able to simulate warm-cloud and cold-cloud formation under a range of controlled environmental conditions through controlled pressure reduction and the resulting adiabatic cooling, thereby

https://doi.org/10.5194/egusphere-2026-3404
Preprint. Discussion started: 10 July 2026

providing a reproducible framework for quantitative seeding experiments. In the warm-cloud experiment, introduction of 10 g of hygroscopic powder increased aerosol number concentration, with maxima at approximately 0.3, 0.7, and 1.5 μm. Relative to the background case, activation started earlier and growth in the 3-10 μm range accelerated; in contrast, the number of droplets ≥12 μm was reduced, consistent with stronger competition for water vapour. The observations are consistent with enhanced condensation and small-droplet growth in the presence of the hygroscopic catalyst, together with reduced production of large droplets. In the cold-cloud experiment, addition of 0.5 g of AgI increased the submicron aerosol number concentration to approximately 2×10^4 cm^{-3}, and was followed by the appearance of identifiable ice-crystal signatures. The AgI-seeded case showed identifiable ice-crystal signatures and a rapid decrease in liquid-droplet concentration, consistent with enhanced ice-phase development under the chamber conditions, reduced the abundance of droplets > 10 μm, and lowered total liquid-droplet concentration, consistent with a shortened cloud lifetime. The observations are consistent with enhanced ice-phase processes after the introduction of AgI-containing aerosol relative to the paired ambient-aerosol background.

Author contributions

JL conducted the experiments, analysed the data, and prepared the manuscript. HZ and YJ assisted with the experiments and data analysis. HW supervised the study and provided guidance on the experimental design and manuscript preparation. All authors reviewed and approved the manuscript.

Competing interests

The contact author has declared that none of the authors has any competing interests.

Acknowledgements

Not applicable.

Financial support

This research has been supported by the Sichuan Provincial Central Leading Local Science and Technology Development Special Project(2025ZYD0179),the “Challenge and Command” China Meteorological Administration(CMA JBGS202607), the Open Grants of China Meteorological Administration Radar Meteorology Key Laboratory (2025ZD02), the Innovation Fund of the Jilin Field Research Station for Cloud Physics, China Meteorological Administration/Jilin Provincial Key Laboratory of Weather Modification (M202504), and the Key Laboratory of Intelligent Meteorological Observation Technology, China Meteorological Administration (ZNGC2025MS21).

https://doi.org/10.5194/egusphere-2026-3404
Preprint. Discussion started: 10 July 2026

Data availability

The dataset is publicly available at https://doi.org/10.17632/6zszgtcdd4.1 (Luo,2025).

References

Al Hosari, T., Al Mandous, A., Wehbe, Y., Shalaby, A., Al Shamsi, N., Al Naqbi, H., Al Yazeedi, O., Al Mazroui, A., and Farrah, S.: The UAE cloud seeding program: A statistical and physical evaluation, Atmosphere, 12, 1013, https://doi.org/10.3390/atmos12081013, 2021.

Andreae, M. and Rosenfeld, D.: Aerosol–cloud–precipitation interactions. Part 1. The nature and sources of cloud-active aerosols, Earth Sci. Rev., 89, 13-41, https://doi.org/10.1016/j.earscirev.2008.03.001, 2008.

Chandrakar, K. K., Cantrell, W., Chang, K., Ciochetto, D., Niedermeier, D., Ovchinnikov, M., Shaw, R. A., and Yang, F.: Aerosol indirect effect from turbulence-induced broadening of cloud-droplet size distributions, Proc. Natl. Acad. Sci. USA, 113, 14243–14248, https://doi.org/10.1073/pnas.1612686113, 2016.

Chang, K., Bench, J., Brege, M., Cantrell, W., Chandrakar, K., Ciochetto, D., Mazzoleni, C., Mazzoleni, L., Niedermeier, D., and Shaw, R.: A laboratory facility to study gas–aerosol–cloud interactions in a turbulent environment: the Π chamber, Bull. Am. Meteorol. Soc., 97, 2343–2358, https://doi.org/10.1175/BAMS-D-15-00203.1, 2016.

Chen, Q., Yin, Y., Jin, L.-j., Xiao, H., and Zhu, S.-c.: The effect of aerosol layers on convective cloud microphysics and precipitation, Atmos. Res., 101, 327-340, https://doi.org/10.1016/j.atmosres.2011.03.007, 2011.

Dias, A., Ehrhart, S., Vogel, A., Williamson, C., Almeida, J., Kirkby, J., Mathot, S., Mumford, S., and Onnela, A.: Temperature uniformity in the CERN CLOUD chamber, Atmos. Meas. Tech., 10, 5075–5088, https://doi.org/10.5194/amt-10-5075-2017, 2017.

Dada, L., Stolzenburg, D., Simon, M., Fischer, L., Heinritzi, M., Wang, M., Xiao, M., Vogel, A. L., Ahonen, L., Amorim, A., Baalbaki, R., Baccarini, A., Baltensperger, U., Bianchi, F., Dällenbach, K., DeVivo, J., Dias, A., Dommen, J., Duplissy, J., et al.: Role of sesquiterpenes in biogenic new particle formation, Sci. Adv., 9, eadi5297, https://doi.org/10.1126/sciadv.adi5297, 2023.

DeMott, P. J.: Quantitative descriptions of ice formation mechanisms of silver iodide-type aerosols, Atmos. Res., 38, 63-99, https://doi.org/10.1016/0169-8095(94)00088-U, 1995.

Fuchs, C., Ramelli, F., Miller, A. J., Omanovic, N., Spirig, R., Zhang, H., Seifert, P., Ohneiser, K., Lohmann, U., and Henneberger, J.: Quantifying ice crystal growth rates in natural clouds from glaciogenic cloud seeding experiments, Atmos. Chem. Phys., 25, 12177-12196, https://doi.org/10.5194/acp-25-12177-2025, 2025.

Gayatri, K., Prabhakaran, T., Malap, N., Konwar, M., Gurnule, D., Bankar, S., and Murugavel, P.: Physical evaluation of hygroscopic cloud seeding in convective clouds using in situ observations and numerical simulations during CAIPEEX, Atmos. Res., 284, 106558, https://doi.org/10.1016/j.atmosres.2022.106558, 2023.

https://doi.org/10.5194/egusphere-2026-3404
Preprint. Discussion started: 10 July 2026

Khain, A., Pinsky, M., Gavze, E., Ronen, A., Elisha, S., Shoshanim, O., and Khain, P.: Warm Fog Elimination by Seeding wit
425 h Salty Drops: Experiments and Theory, J. Weather Modif., 55, 30-51, https://doi.org/10.2139/ssrn.4309435, 2024.
Kirkby, J., Amorim, A., Baltensperger, U., Carslaw, K. S., Christoudias, T., Curtius, J., Donahue, N. M., El Haddad, I., Flaga n, R. C., Gordon, H., Hansel, A., Harder, H., Junninen, H., Kulmala, M., Kürten, A., Laaksonen, A., Lehtipalo, K., Lelieveld, J., Möhler, O., et al.: Atmospheric new particle formation from the CERN CLOUD experiment, Nat. Geosci., 16, 948-957, https://doi.org/10.1038/s41561-023-01305-0, 2023.
430 Kim, B.-Y., Belorid, M., Cha, J. W., Kim, Y., and Kim, S.: Analysis of hygroscopic cloud seeding materials using the Korea C loud Physics Experimental Chamber (K-CPEC): a case study for powder-type sodium chloride and calcium chloride, Atmos. Meas. Tech., 18, 3781–3797, https://doi.org/10.5194/amt-18-3781-2025, 2025.
Knowles, S. and Skidmore, M.: Cloud seeding and crops yields: evaluation of the North Dakota cloud modification project, Weather Clim. Soc., 13, 885-898, https://doi.org/10.1175/WCAS-D-21-0010.1, 2021.
435 Koo, H.-J., Chang, K.-H., Chae, S., Cha, J. W., Hwang, H., Kim, M.-H., Ku, J. M., Lim, Y.-K., Jung, W., and Lee, Y. H.: A su ggestion of verification method for cloud seeding experimental results via analyses of chemical components of precipitation, J. Appl. Meteorol. Clim., 64, 497–512, https://doi.org/10.1175/JAMC-D-23-0212.1, 2025.
Kuba, N. and Murakami, M.: Effect of hygroscopic seeding on warm rain clouds–numerical study using a hybrid cloud micro physical model, Atmos. Chem. Phys., 10, 3335-3351, https://doi.org/10.5194/acp-10-3335-2010, 2010.
440 Kuo, W.-C., Yamashita, K., Murakami, M., Tajiri, T., and Orikasa, N.: Numerical simulation on feasibility of rain enhanceme nt by hygroscopic seeding over Kochi area, Shikoku, Japan, in early summer, J. Meteorol. Soc. Jpn. Ser. II, 102, 429-443, https://doi.org/10.2151/jmsj.2024-021, 2024.
Li, D., Zhao, C., Li, P., Liu, C., Gong, D., Liu, S., Yuan, Z., and Chen, Y.: Macro-and micro-physical characteristics of differe nt parts of mixed convective-stratiform clouds and differences in their responses to seeding, Adv. Atmos. Sci., 39, 2040-2055,
445 https://doi.org/10.1007/s00376-022-2003-8, 2022.
Lüttmer, T., Spichtinger, P., and Seifert, A.: Investigating ice formation pathways using a novel two-moment multi-class clou d microphysics scheme, Atmos. Chem. Phys., 25, 4505-4529, https://doi.org/10.5194/acp-25-4505-2025, 2025.
Miller, A. J., Fuchs, C., Ramelli, F., Zhang, H., Omanovic, N., Spirig, R., Marcolli, C., Kanji, Z. A., Lohmann, U., and Henne berger, J.: Quantified ice-nucleating ability of AgI-containing seeding particles in natural clouds, Atmos. Chem. Phys., 25, 53
450 87-5407, https://doi.org/10.5194/acp-25-5387-2025, 2025.
Morrison, H., van Lier-Walqui, M., Fridlind, A. M., Grabowski, W. W., Harrington, J. Y., Hoose, C., Korolev, A., Kumjian, M. R., Milbrandt, J. A., and Pawlowska, H.: Confronting the challenge of modeling cloud and precipitation microphysics, J. Ad v. Model. Earth Syst., 12, e2019MS001689, https://doi.org/10.1029/2019MS001689, 2020.
Mossop, S. C.: AgI-NaI aerosols as ice nuclei in a laboratory cloud chamber, J. Appl. Meteorol., 8, 241-248, https://doi.org/1
455 0.1175/1520-0450(1969)008<0241:ANAAIN>2.0.CO;2, 1969.
Murphy, D. M. and Koop, T.: Review of the vapour pressures of ice and supercooled water for atmospheric applications, Q. J. R. Meteorol. Soc., 131, 1539–1565, https://doi.org/10.1256/qj.04.94, 2005.

https://doi.org/10.5194/egusphere-2026-3404
Preprint. Discussion started: 10 July 2026

Murray, B., O'sullivan, D., Atkinson, J., and Webb, M.: Ice nucleation by particles immersed in supercooled cloud droplets, Chem. Soc. Rev., 41, 6519-6554, https://doi.org/10.1039/C2CS35200A, 2012.

Padmakumari, B., Maheskumar, R., Morwal, S., and Kulkarni, J.: Variability of Index of Coalescence Activity (ICA) over a rain-shadow region during monsoon and its role in cloud seeding programs in India, Atmos. Res., 304, 107390, https://doi.org/10.1016/j.atmosres.2024.107390, 2024.

Park, M., Cha, J. W., Park, S., Kim, J., Kim, Y., Belorid, M., Kim, B.-Y., Baek, J., Kim, S., and Lee, K.: Introduction to the Korea Cloud Physics Experimental Chamber (K-CPEC), Bull. Am. Meteorol. Soc., 106, E1897–E1918, https://doi.org/10.1175/BAMS-D-24-0330.1, 2025.

Rosenfeld, D., Axisa, D., Woodley, W. L., and Lahav, R.: A quest for effective hygroscopic cloud seeding, J. Appl. Meteorol. Clim., 49, 1548–1562, https://doi.org/10.1175/2010JAMC2307.1, 2010.

Schnaiter, M., Järvinen, E., Vochezer, P., Abdelmonem, A., Wagner, R., Jourdan, O., Mioche, G., Shcherbakov, V. N., Schmitt, C. G., Tricoli, U., Ulanowski, Z., and Heymsfield, A. J.: Cloud chamber experiments on the origin of ice crystal complexity in cirrus clouds, Atmos. Chem. Phys., 16, 5091–5110, https://doi.org/10.5194/acp-16-5091-2016, 2016.

Schnitzhofer, R., Metzger, A., Breitenlechner, M., Jud, W., Heinritzi, M., De Menezes, L.-P., Duplissy, J., Guida, R., Haider, S., Kirkby, J., Mathot, S., Minginette, P., Onnela, A., Walther, H., Wasem, A., Hansel, A., and the CLOUD Team: Characterisation of organic contaminants in the CLOUD chamber at CERN, Atmos. Meas. Tech., 7, 2159–2168, https://doi.org/10.5194/amt-7-2159-2014, 2013.

Shaw, R. A., Chen, S., Freer, M., Korolev, A., Krueger, S., Murakami, M., Niedermeier, D., Ovchinnikov, M., Schmalfuß, S., and Tian, P.: Scientific directions for cloud chamber research: instrumentation, modeling, new chambers, and emerging chamber concepts, Bull. Am. Meteorol. Soc., 106, E770–E781, https://doi.org/10.1175/BAMS-D-25-0027.1, 2025.

Shen, J., Russell, D. M., DeVivo, J., Kunkler, F., Baalbaki, R., Mentler, B., Scholz, W., Yu, W., Caudillo-Plath, L., Sommer, E., Ahongshangbam, E., Alfaouri, D., Almeida, J., Amorim, A., Beck, L. J., Beckmann, H., Berntheusel, M., Bhattacharyya, N., Canagaratna, M. R., et al.: New particle formation from isoprene under upper-tropospheric conditions, Nature, 636, 115-123, https://doi.org/10.1038/s41586-024-08196-0, 2024.

Silverman, B. A.: A critical assessment of hygroscopic seeding of convective clouds for rainfall enhancement, Bull. Am. Meteorol. Soc., 84, 1219–1230, https://doi.org/10.1175/BAMS-84-9-1219, 2003.

Silverman, B. A. and Sukarnjanaset, W.: Results of the Thailand Warm-Cloud Hygroscopic Particle Seeding Experiment, J. Appl. Meteorol., 39, 1160–1175, https://doi.org/10.1175/1520-0450(2000)039<1160:ROTTWC>2.0.CO;2, 2000.

Su, Z., Guo, X., Jie, Z., and Wang, P.: Developing and testing of an expansion cloud chamber for cloud physics research, J. Appl. Meteorol. Sci., 30, 722-730, https://doi.org/10.11898/1001-7313.20190608, 2019.

Tajiri, T., Yamashita, K., Murakami, M., Saito, A., Kusunoki, K., Orikasa, N., and Lilie, L.: A novel adiabatic-expansion-type cloud simulation chamber, J. Meteorol. Soc. Jpn. Ser. II, 91, 687-704, https://doi.org/10.2151/jmsj.2013-509, 2013.

Tajiri, T., Yamashita, K., Saito, A., and Murakami, M.: MRI cloud chamber experiments: cloud condensation nuclei and ice nuclei abilities of cloud seeding materials, Earozoru Kenkyu, 30, 14-23, https://doi.org/10.11203/jar.30.14, 2015.

https://doi.org/10.5194/egusphere-2026-3404
Preprint. Discussion started: 10 July 2026

Tessendorf, S. A., Chen, S., Weeks, C., Bruintjes, R., Rasmussen, R. M., and Xue, L.: The influence of hygroscopic flare seeding on drop size distribution over southeast Queensland, J. Geophys. Res. Atmos., 126, e2020JD033771, https://doi.org/10.1029/2020JD033771, 2021.

Thomas, L., Yang, F., Wang, A., Ovchinnikov, M., Pressel, K. G., and Shaw, R. A.: Enhancing turbulent mixing and microphysical uniformity in a tall convection-cloud chamber through idealized heterogeneity of boundaries, J. Adv. Model. Earth Syst., 17, e2025MS005316, https://doi.org/10.1029/2025MS005316, 2025.

Thomas, S., Yang, F., Ovchinnikov, M., Cantrell, W., and Shaw, R. A.: Scaling of turbulence and microphysics in a convection–cloud chamber of varying height, J. Adv. Model. Earth Syst., 15, e2022MS003304, https://doi.org/10.1029/2022MS003304, 2023.

Tonttila, J., Korpinen, A., Kokkola, H., Romakkaniemi, S., Fortelius, C., and Korhonen, H.: Interaction between hygroscopic seeding and mixed-phase microphysics in convective clouds, J. Appl. Meteorol. Clim., 61, 1533–1547, https://doi.org/10.1175/JAMC-D-21-0183.1, 2022.

Wagner, R., Möhler, O., Saathoff, H., Schnaiter, M., and Leisner, T.: New cloud chamber experiments on the heterogeneous ice nucleation ability of oxalic acid in the immersion mode, Atmos. Chem. Phys., 11, 2083-2110, https://doi.org/10.5194/acp-11-2083-2011, 2011.

Wang, F., Li, Z., Jiang, Q., Wang, G., Jia, S., Duan, J., and Zhou, Y.: Evaluation of hygroscopic cloud seeding in liquid-water clouds: a feasibility study, Atmos. Chem. Phys., 19, 14967-14977, https://doi.org/10.5194/acp-19-14967-2019, 2019.

Wang, Y., Chai, T., Li, J., Feng, L., Jian, J., Huang, J., and McFarquhar, G. M.: Dust decline amplifies high-cloud ice-to-liquid transition and buffers the radiative feedback under warming, Geophys. Res. Lett., 53, e2026GL121917, https://doi.org/10.1029/2026GL121917, 2026.

Wu, X., Yan, N., Yu, H., Niu, S., Meng, F., Liu, W., and Sun, H.: Advances in the evaluation of cloud seeding: Statistical evidence for the enhancement of precipitation, Earth Space Sci., 5, 425-439, https://doi.org/10.1029/2018EA000424, 2018.